International Journal of Heat and Mass Transfer 163 (2020) 120474

Contents lists available at ScienceDirect

International Journal of Heat and Mass Transfer

journal homepage: www.elsevier.com/locate/hmt

Thin liquid films formation and evaporation mechanisms around elongated bubbles in rectangular cross-section microchannels

Meisam Habibi Matin, Saeed Moghaddam*

Department of Mechanical and Aerospace Engineering, University of Florida, Gainesville, FL 32611, United States

ARTICLE INFO

Article history:
Received 5 July 2020
Revised 12 September 2020
Accepted 13 September 2020
Available online 24 September 2020

Keywords:
Thin liquid films
Flow boiling
Microchannels
Channel aspect ratio

ABSTRACT

Thin film evaporation is the dominant mechanism of heat transfer in the microchannel flow boiling process. Hence, its understanding is paramount to development of predictive models and more efficient microchannel heat exchangers. Although microchannels mostly have a rectangular cross-section, the existing models are developed for circular cross-section microchannels. The non-uniformity of the liquid film thickness in microchannels with a rectangular cross-section has made prediction of the onset of dryout and heat transfer coefficient greatly challenging. Here, a test device capable of measuring the wall heat flux is utilized to fully characterize the thin film formation and evaporation process. The effects of flow capillary number (Ca) and channel aspect ratio on the liquid film thickness are determined in microchannels with 300 μm width and 300, 150, and 75 μm heights, representing aspect ratios of 1, 2, and 4, respectively. It is shown that the only existing mechanistic model for the elongated bubble regime in microchannels fails to predict the experimental heat transfer coefficient (HTC) both quantitively, by a 50–120% margin, and qualitatively, due to a fundamental difference in evaporation and dryout of a variable versus a uniform film assumed in the model. The results presented here pave the way for development of a more accurate mechanistic model for the thin film evaporation heat transfer mechanism in microchannels with a rectangular cross-section.

1. Introduction

Flow boiling and its associated heat transfer mechanisms in microchannels have been the subject of numerous studies [1–10]. Models with fundamentally different assumptions about the process physics have been proposed [11–15]. The first set of models are those developed based on the superimposed concept originally presented for macrochannels [11,12]. The fundamental assumption of these models is that convection (both micro- and macroconvection) is the primary mode of heat transfer in microchannels. The second set of models assume that direct evaporation of thin liquid films is the dominant mechanism of heat transfer [13–15]. Historically, performance of these models has been assessed by their ability to predict the overall surface heat transfer coefficient, which is the cumulative effect of a set of boiling heat transfer sub-processes. Although multiple mechanisms are responsible for heat transfer, recent direct measurement of all mechanisms of heat transfer [16,17] have confirmed that thin film evaporation is the primary mechanism of heat transfer. Thin liquid films with thicknesses on the order of micrometers form around elongated bubbles or a vapor core. These films may be stationary at low vapor velocities (i.e. the elongated bubble regime) but can flow and become unstable and rupture/atomize at high vapor velocities during transition from one flow regime to another [18].

Thome et al. [15] proposed a model for heat transfer coefficient (HTC) considering the thin film evaporation mechanism as the prominent mode of heat transfer. The model considers three zones with distinct heat transfer characteristics associated with; evaporation of a thin liquid film around an elongated bubble, a dry vapor plug with negligible heat transfer, and a liquid slug with a relatively low (i.e. single-phase level) heat transfer. For the initial thickness of the liquid film, Thome et al. [15] used an empirical thin film thickness model experimentally determined by Moriyama and Inoue [19]. Moriyama and Inoue [19] determined the thickness of a liquid film of R-113 formed between a vapor bubble growing radially in a gap between two parallel glass substrates. They measured temperature of the bottom surface of the lower substrate using radially distributed thermocouples and utilized the temperature values to numerically solve the heat conduction equation within the glass substrate. They then used equation $\delta = q''.dt/\rho h_{fg}$ to calculate the initial thickness of the liquid film formed between the bubble and the glass substrate. The three-zone model has recently been updated [20] using a new empirical correlation for the

* Corresponding author.
E-mail address: saeedmog@ufl.edu (S. Moghaddam).

https://doi.org/10.1016/j.ijheatmasstransfer.2020.120474
0017-9310/

Nomenclature

Ca	Capillary number
H	channel height
h	heat transfer coefficient
h_{fg}	latent heat of vaporization
k	thermal conductivity
Re	Reynolds number
$q"$	heat flux
T	temperature
T_{sat}	saturation temperature
T_s	temperature at SU8-liquid interface
T_{Si-SU8}	temperature at Si-SU8 interface
ΔT	temperature difference, $T_{Si-SU8} - T_s$
t	time
U	bubble velocity
W	channel width

Greek Symbols

δ_0	initial film thickness
δ_H	film thickness on the channel side wall
δ_V	film thickness on the channel bottom wall
ρ	liquid density
ν	liquid kinematic viscosity
μ	liquid dynamic viscosity
σ	surface tension
α	aspect ratio, W/H

initial film thickness proposed by Han and Shikazono [21] for adiabatic flow in circular cross-section microchannels. The proposed empirical correlation was later updated by Han et al. [22] to account for bubbles acceleration, due to liquid evaporation.

Since the surface tension and viscous forces dominate the force field within the thin liquid film formed around an elongated bubble, the capillary number ($Ca = \mu U/\sigma$) which represents the balance of these forces is the key parameter dictating the liquid film thickness. Development of models relating the liquid film thickness to Ca dates back to several decades ago [23–28]; notably, to the work of Bretherton [23] who related the liquid film thickness to Ca as $\delta/R = 1.34Ca^{2/3}$ (for $Ca < 0.003$), wherein δ is the film thickness and R is the channel radius, using the planar (i.e. 1-D) lubrication equation (i.e. a balance between the viscous force and the pressure gradient along a dynamic meniscus). Subsequent models have emanated from Bretherton's formulation [23] with modifications proposed to; for example, extend its range to higher Ca by Aussillous and Quere´ [27] and account for the effect of inertia by Han and Shikazono [21]. Others have used the Bretherton's formula to evaluate the interfacial shear effects on evaporating liquid films [29,30]. Although these models are useful for microchannels with a circular cross-section (Fig. 1A), they cannot be used for microchannel heat sinks that are made predominantly with a rectangular cross-section channels.

In microchannels with square and rectangular cross-sections, the liquid film thickness varies circumferentially due to the channel corners and the non-uniform peripheral pressure distribution in the liquid [25,31–35]. In a square cross-section, although the liquid at the corners (i.e., gutters) makes it difficult to determine the liquid film distribution, the bubble cross-section is still symmetric across the diagonal axis and the liquid film thickness on all walls is the same (Fig. 1B). However, in a rectangular cross-section, the liquid film thickness is different along each channel axis (Fig. 1C, D) and it also depends on the confinement degree (i.e., channel aspect ratio, α). Intuitively, confinement in a rectangular channel squeezes a bubble into a non-axisymmetric cross-section shape while surface tension force acts to restore the vapor-liquid

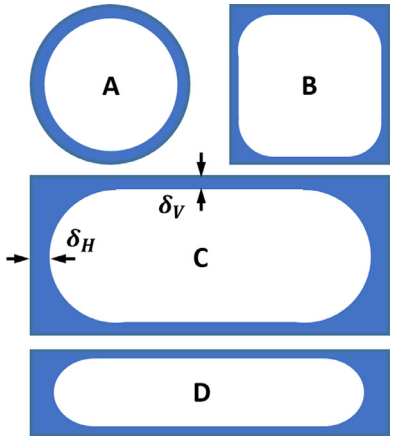

Fig. 1. Depiction of the liquid film distribution around a bubble in microchannels with different cross-sections: (A) Circular, (B) Square (α=1), (C) Rectangular with a low aspect ratio (α=2), (D) Rectangular with a high aspect ratio (α=4).

interface to the axisymmetric state. Hence, increasing the α results in thickening of the liquid film on the side wall of the channel (δ_H), while squeezing the liquid film on the bottom and top walls (δ_v) (compare Figs. 1C and B). A body of fluid dynamics literature concerning adiabatic propagation of air fingers into rectangular tubes filled with a liquid provides valuable insight into physics of liquid films formation on periphery of rectangular cross-section channels. In complementary numerical simulations, Hazel and Heil [31] and de Lozar et al. [36] showed that as Ca increases, the fluid film thickens and in near-square channels the ultimate finger shape becomes axisymmetric at sufficiently high Ca. However, axisymmetric configurations are possible for $\alpha < 2.04$ but never occurs for $\alpha > 2.04$ [31,36]. Instead, the equilibrium finger shape consists of end regions of constant curvature connected by liquid films along the longer walls of the channel (the study provides details for $Ca = 1.0$ and $\alpha = 3, 7$). Hazel and Heil [31] further demonstrated that at sufficiently low capillary numbers changes in δ_v with capillary is significantly small relative to changes in δ_H.

Recently, in a comprehensive experimental and numerical study [37], we showed that surface temperature and heat flux measurements by a microsensor array can be used to determine the liquid film thickness in rectangular cross-section microchannels. In the present study, we have enhanced the microsensors spatial resolution across the microchannel width and conducted a series of studies to determine the liquid film profile and evaporation rate as well as progression of the surface dry-out. Also, to study the effect of microchannel aspect ratio on these phenomena, three microchannels with a width of 300 μm and heights of 300, 150 and 75 μm, corresponding to aspect ratios α =1, 2 and 4, respectively, are fabricated. In the following sections, we first describe development of devices with the new microsensors layout. Then, spatial and temporal variations of the surface heat flux as a function of flow Ca, bubble length, and channel aspect ratio are discussed. It is then explained how the heat flux results are utilized to determine the liquid film thickness, and comparisons are made with the existing literature. Finally, the measured local and average heat transfer coefficients are compared with predictions of the three-zone model [20].

2. Experimental setup

2.1. Test device

The devices are microfabricated on a 500-μm-thick silicon (Si) wafer with a 12-μm-thick SU8 polymer layer (Fig. 2A). A total of

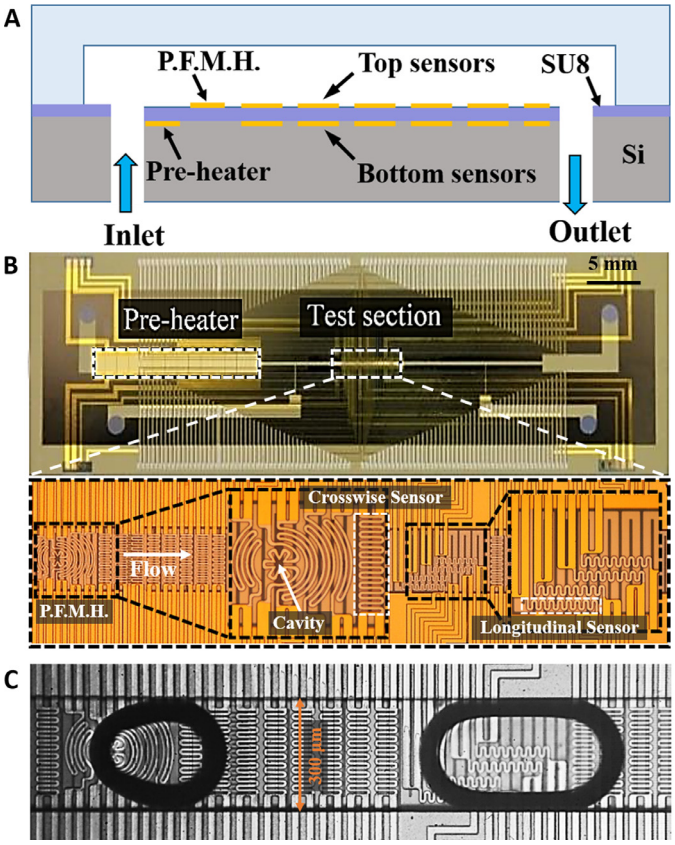

Fig. 2. (A) A 2-D schematic of the microfluidic device cross-section, (B) A detailed view of the microfluidic chip with the enlarged view of the test section (shwoing pre-heater, crosswise sensors, longitudinal sensors, nucleation cavity, and pulsed function microheater (PFMH)), (C) Bubbles are generated by the PFMH and flow through the microchannel.

50 resistance temperature detectors (RTDs) are microfabricated at the Si–SU8 and SU8–fluid interfaces (Fig. 2A) through deposition of a 100-nm-thick platinum film. The RTDs are oriented in the longitudinal and crosswise directions (Fig. 2B). These longitudinal and crosswise sensors are 30 μm and 60 μm wide, respectively; placed 15 μm apart from their neighboring sensors. To increase the temperature measurement accuracy, the 4-wire configuration is utilized, i.e. each sensor has four connections (excitation ± and readout ±). Microheaters fabricated on the Si surface maintain the channel wall at desired temperatures. The chip is equipped with a microfabricated pre-heater section to heat the working fluid (FC-72, 3M^{TM} Fluorinert^{TM}) to a desired temperature before arriving at the test section (Fig. 2A). Bubbles are generated at the beginning of the test section by a pulsed function microheater (PFMH) fabricated on the SU8 film (Fig. 2B). To control the nucleation site, a 300 nm in diameter dedicated cavity (Fig. 2B) was fabricated at the middle of the microheater using a focused ion beam (FIB) milling machine (Fig. 2B). Three microchannels with cross-sections 300 × 300 μm^2, 150 × 300 μm^2 and 75 × 300 μm^2 were made from polydimethylsiloxane (PDMS) and then bonded over the sensor array chips using oxygen plasma bonding. Each microfluidic chip was wire bonded to a custom-made, double-sided printed circuit board (PCB). Fig. 2C shows a top view image of the 300 × 150 μm^2 channel during a test.

2.2. Test loop and data collection

Fig. 3 depicts the experimental setup. All RTD sensors connections are directed to a separate ribbon socket and routed to a data acquisition (DAQ) system. The DAQ system, which consists of a current excitation module (NI SCXI-1581), a channel amplifier module (i.e., signal conditioning module) (NI SCXI-1120C), a high speed DAQ module (NI PXI-6289), and a programmable DC power supply module (NI PXI-4110), is commanded by an embedded controller (NI PXI-8115). The PFMH is connected to the programmable DC power supply module. The temperature data are recorded at 20 kHz frequency. All data collection, including the control for the applied DC voltage of the PFMH, is performed using a LabVIEW program. The thin film heaters are also powered by the NI PXI-4110 DC power supply. A high-speed camera (FASTCAM SA4-Photron) is synchronized with the DAQ to visualize the boiling process at a frequency of 10k frames/s. The working fluid is delivered to the microfluidic chip by a piezoelectric micropump (Model MP6, manufactured by Bartels Mikrotechnik GmbH). Then, the desired surface temperature is adjusted and allowed about 20 min to reach steady state before recording the data.

2.3. Sensor calibration and uncertainty analysis

The RTD sensors are calibrated to obtain the voltage–temperature (V-T) relationship of each sensor. The calibration tests are conducted in a uniform temperature oven at a temperature range of 40 °C to 90 °C. A constant current excitation of 100 μA is supplied to each sensor. The obtained V-T curves show a linear trend and the sensitivity of the RTD sensors is 0.22 mV.°C^{-1}. The data acquisition system has a maximum uncertainty of ±28 μV, at a gain of 100 with a minimum detectable voltage change of 1 μV. Considering the sensitivity of the sensors and the voltage uncertainty, the maximum error in temperature measurements is determined to be ±0.15 °C. In addition, the maximum uncertainty in the measurement of the SU8 film thickness is ±0.01 μm. The temperature sensors self-heating is negligible.

The temperature uncertainty propagates into the heat flux data, heat transfer coefficient, and liquid film thickness. Uncertainty in the local heat flux data can be calculated as follows:

$$\frac{\delta q''}{q''} = \sqrt{\left(\frac{\delta T}{T}\right)^2 + \left(\frac{\delta(\Delta y)}{\Delta y}\right)^2} \tag{1}$$

where Δy is thickness of the SU8 layer. Maximum uncertainty in measurement of SU8 film thickness is ±0.01 μm. The uncertainty of the two-phase heat transfer coefficient is estimated as:

$$\frac{\delta h_{T.Ph.}}{h_{T.Ph.}} = \sqrt{\left(\frac{\delta q''}{q''}\right)^2 + \left(\frac{\delta(\Delta T)}{(\Delta T)}\right)^2} \tag{2}$$

where $\Delta T = T - T_{sat}$. Uncertainty in δ_v is approximated using the following expression:

$$\frac{\delta(\delta_V)}{\delta_V} = \sqrt{\left(\frac{\delta q''}{q''}\right)^2 + \left(\frac{\delta(\Delta T)}{(\Delta T)}\right)^2} \tag{3}$$

The maximum uncertainties in measurement of the heat flux and the heat transfer coefficient are 0.7 W/cm^2, 3.5 kW/m^{2}K, respectively.

3. Results and discussion

In a typical experiment, single bubbles are generated at a desired rate by adjusting the frequency and amplitude of the voltage applied to the PFMH surrounding the nucleation site. The bubble length and velocity are controlled by adjusting the surface temperature and mass flux. As a bubble moves along the microchannel, the sensors measure the Si-SU8 and SU8-fluid interface temperatures. As shown in Habibi Matin et al. [37], the Si-SU8 interface

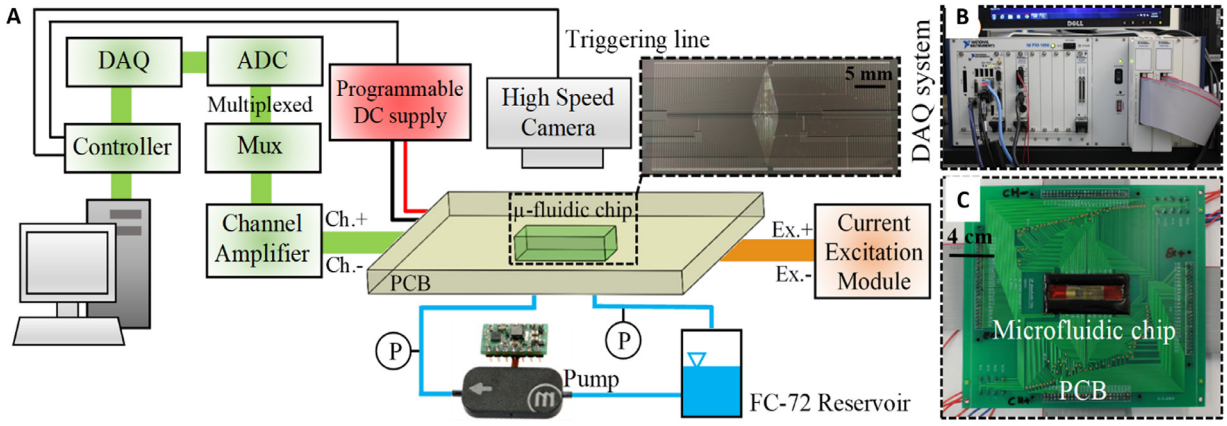

Fig. 3. (A) A schematic of the experimental setup, (B) An image of DAQ system, (C) An image of the microfluidic chip wire bonded to a custom-made double-sided printed circuit board (PCB).

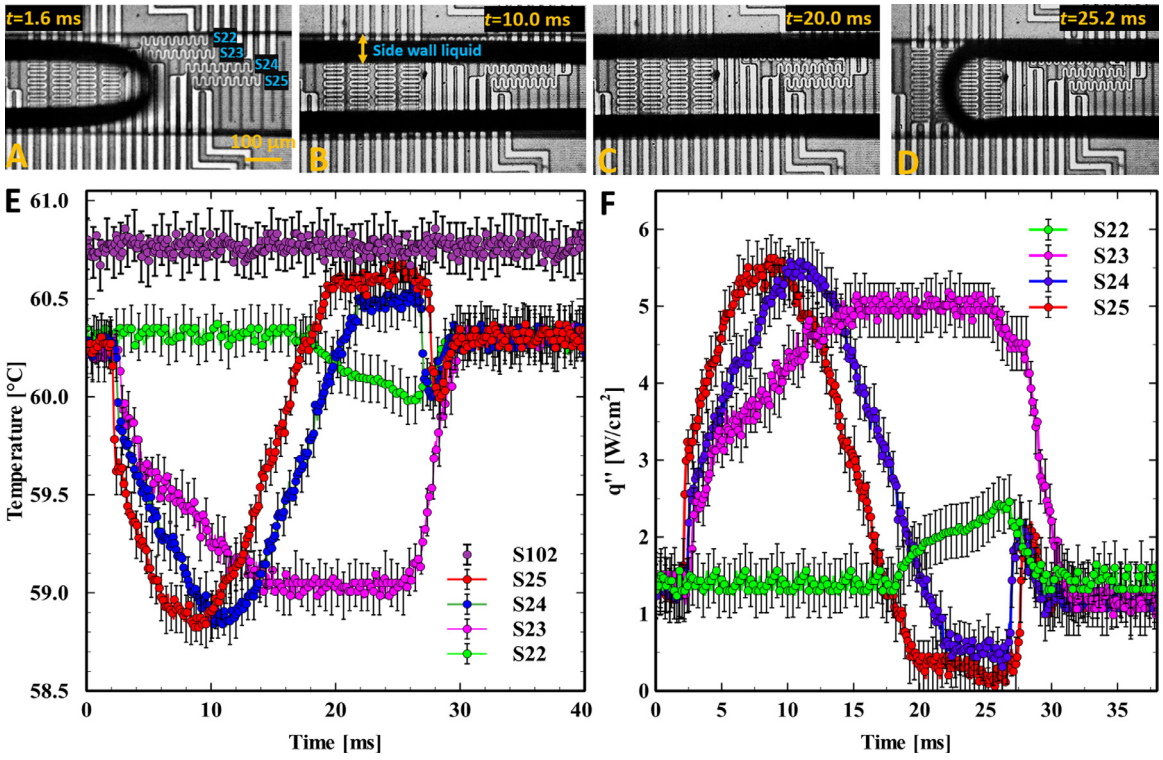

Fig. 4. Data recorded using a high-speed camera and sensors S22-S25 for a bubble at Ca =0.032 flowing in the microchannel with α = 2: (A-D) Bubble passes over the sensor causing liquid film formation and partial dryout, (E) Temperature values recorded as a function of time, (F) Local heat flux values corresponding to the recorded temperatures (t =0 is an arbitrary time that marks passage of this particular bubble over the sensing area).

temperature remains uniform due to the high thermal conductivity of Si. The heat flux is then calculated using the difference in temperature of the two interfaces, i.e. $q'' = \Delta T(k_{SU8}/\delta_{SU8})$. Fig. 4 shows images of a representative bubble along with the synchronized temperature and heat flux data for a microchannel with an aspect ratio (α) of 2. The reference time (i.e. t =0) is arbitrary marking the passage of this particular bubble over the sensors array, selected from among hundreds of similar events recorded during a few seconds.

3.1. Surface thermal field during liquid film evaporation

Fig. 4A shows when (t = 1.6 ms) the bubble is about to move over longitudinal sensors S22–S25 (located at the SU8-fluid interface). The bubble leading edge moves, at a velocity of 0.52 m/s, over the sensors in ~0.35 ms. The bubble arrival on sensors S22-S25 triggers a set of heat transfer events, as shown in Fig. 4E, F (S102 measures the Si-SU8 interface temperature). Temperatures of sensors S25 and S24 simultaneously drop (i.e. heat flux rises) at t = 2 ms and remain low long after the leading edge of the bubble passes over the sensors, while the "apparent contact line" associated with the liquid layer formed on the microchannel sidewalls resides on S23. This cooling event is caused by direct evaporation of a liquid film formed over the sensors. The lower rate of increase in heat flux (dq''/dt) on S24 relative to S25 is due to the formation of a thicker liquid film on S24 in an otherwise identical heat transfer event (i.e. rise and fall of heat flux) over the two sensors. Another evidence of a thicker liquid film formed on S24 is the higher overall heat transfer (i.e. integral of the heat flux over time) compared to that of S25. The dq''/dt on S23 is further slowed, relative to that of S24 and S25, not only due to a thicker liquid film but

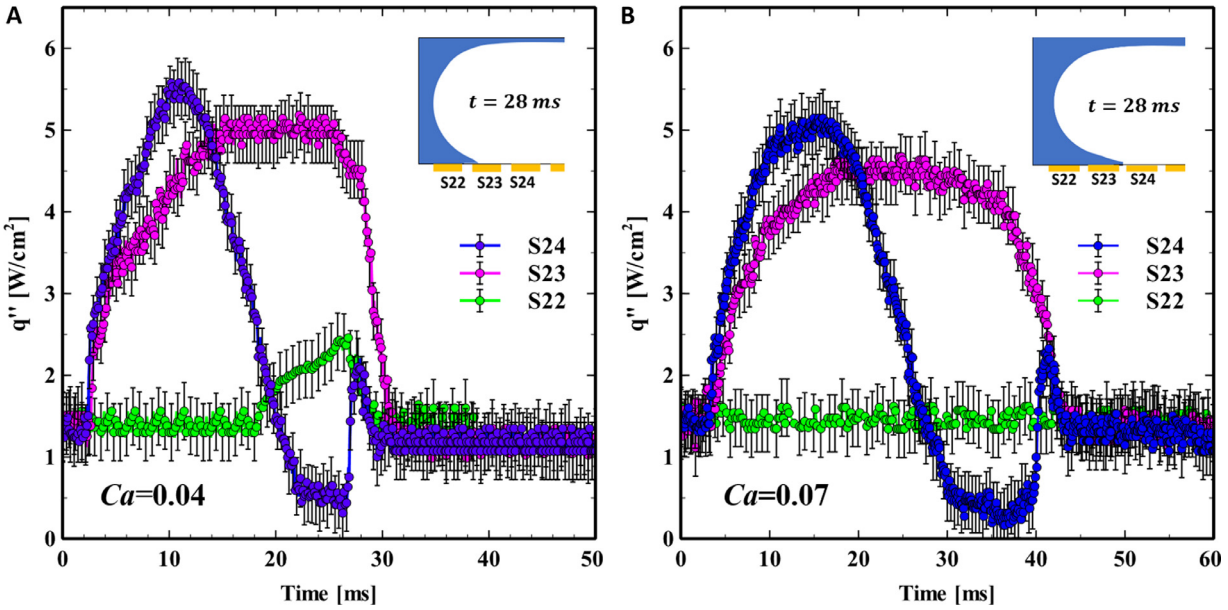

Fig. 5. Local heat flux signatures for sensors S22-S24 at (A) $Ca = 0.04$ and (B) $Ca = 0.07$ (the insets illustrate the contact line position at an arbitrary time).

also partial coverage by the thick liquid layer formed on the microchannel sidewall. The latter reason is supported by readings of sensor S22 which shows no change in the heat flux during much of S25, S24, and S23 rapid cooling period until t =16 ms when a moderate rise in heat flux occurs suggesting that the apparent contact line has moved near or over S22, from above S23. Therefore, although sensor S22 encounters the bubble prior to other sensors, it does not experience a temperature drop (i.e., heat flux increase) at the bubble arrival (until t =16 ms) because there is a column of liquid above the sensor i resulting in single-phase heat transfer to the bulk liquid. The presence of the apparent contact line on sensor S23 produced a distinct heat flux signature, quasi-steady for 10 ms (from t =16 ms to 26 ms), through continuous feeding of the evaporating liquid film by the liquid layer formed on the channel sidewall.

This quasi-steady cooling event is truncated when the trailing edge of the bubble arrives over S23 at $t = 26$ ms, and the heat flux rapidly descends to a value equal to that of sensors S22, S24, and S25 at $t = 28$ ms. The sensors recordings of this remarkable event suggest that the entire surface is subjected to the same boundary condition (i.e. heat transfer coefficient). Sensors S25 and S24 that have almost dried out (i.e. experiencing a near zero heat transfer coefficient) are quenched by the liquid front. Sensor S22 that just started experiencing cooling due to the direct evaporation of the sidewall's liquid encounters the same transient heat transfer mechanism; evidently, with a lower heat transfer coefficient. This mechanism has been identified and modeled in our prior study [16] as the transient conduction mechanism of heat transfer, caused by a mismatch between the liquid and surface temperatures. This heat transfer event subsided rapidly, over a 3-4 ms period, after which heat transfer to the liquid slug dominated the surface cooling process beyond $t = 30$ ms, until the next bubble passed over the sensors.

3.2. *Effect of* Ca *on surface thermal field*

Fig. 5 compares the surface heat flux associated with the liquid film evaporation events on sensors S23 and S24 for $Ca = 0.04$ (Fig. 5A) and 0.07 (Fig. 5B). Comparison of the results for these two test conditions clearly shows a longer cooling event at $Ca = 0.07$ relative to that of 0.04. Given that the area under the heat flux curve represents the overall energy removed from the surface, it can be readily concluded that the liquid film thickness over the microchannel bottom wall has increased with Ca. The heat flux data of S22 also confirms formation of a thicker liquid film over the microchannel sidewalls for a higher Ca flow condition. This conclusion is reached considering that the continuous evaporation of a thinner sidewall liquid at $Ca = 0.04$ has ultimately led to the recession of the apparent contact line to near or over the S22 sensor, leading to a rise in heat flux beginning at $t = 16$ ms (Fig. 5A). In contrast, S22 does not experience any variation in heat flux in the case of $Ca = 0.07$ (Fig. 5B) indicating the presence of a thicker liquid film over the sidewall that has yet to sufficiently evaporate such that the apparent contact line could recede over the S22 sensor.

3.3. *Effect of bubble length on liquid film evaporation and dryout*

The thin film evaporation events discussed in the previous sections do not apply to all bubbles – fundamentally different thin film evaporation events can ensue when elongated bubbles with different sizes flow through the microchannel. The previously discussed bubbles were long enough to allow full evaporation of the liquid film followed by a period of dryout. However, the liquid film does not fully evaporate when bubbles are too short. To highlight this phenomenon, we compare the thin film evaporation process associated with a long, a short, and a medium size bubble. It should be noted that this classification intends to provide a qualitative assessment of the effect of bubbles' lenght on evaporation of the liquid films , and it is merely an attempt to show that contrary to the assumptions of the three-zone model, bubbles of various sizes dictate the extent of liquid film evaporation and whether the surface experiences dryout. Fig. 6 provides the temperature and heat flux values on sensor S23 in $\alpha = 2$ channel as different size bubbles pass over the sensor. The experiment was conducted in a way that Ca number for all bubbles is the same ($i.e.\ Ca = 0.03$).

As the results suggest, in the case of a short bubble, the thin film evaporation process is terminated prematurely resulting in recovery of the surface temperature (Fig. 6A) and a decline in heat flux (Fig. 6B) shortly after the process starts, at $t = 6$ ms. The arrival of a liquid slug over S23 established a constant surface heat flux, associated with heat transfer to the bulk liquid flow. Also,

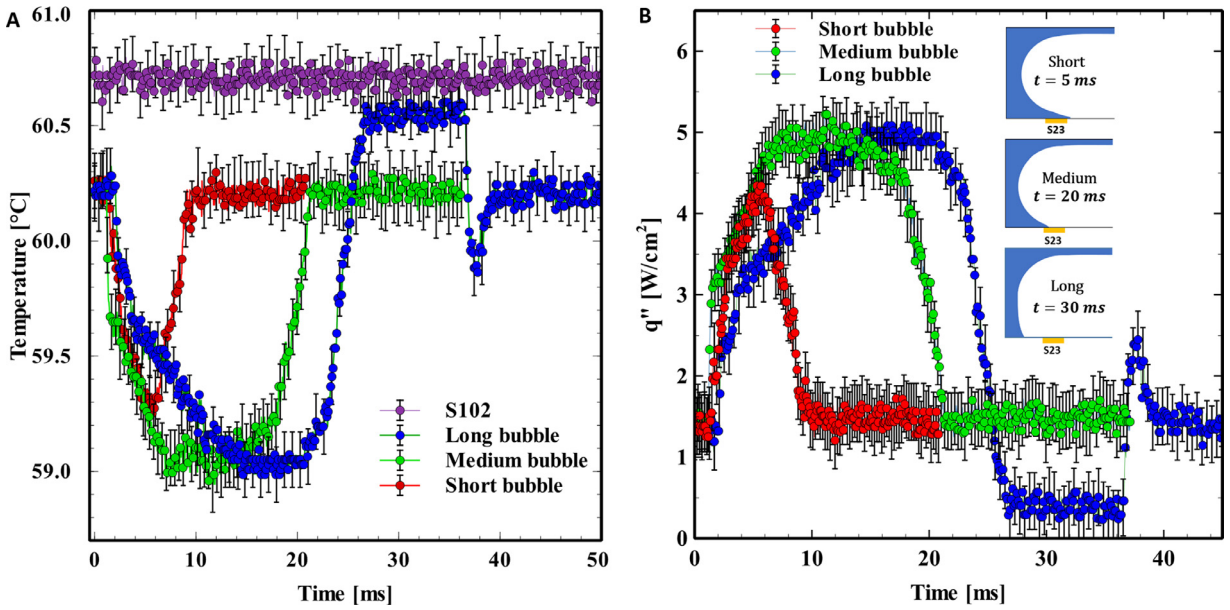

Fig. 6. (A) Temperature signature recorded by sensors S23 and S102, and (B) Local heat flux values obtained using temperature data for bubbles with different sizes passing over the sensor (the insets illustrate the contact line position at an arbitrary time for each bubble).

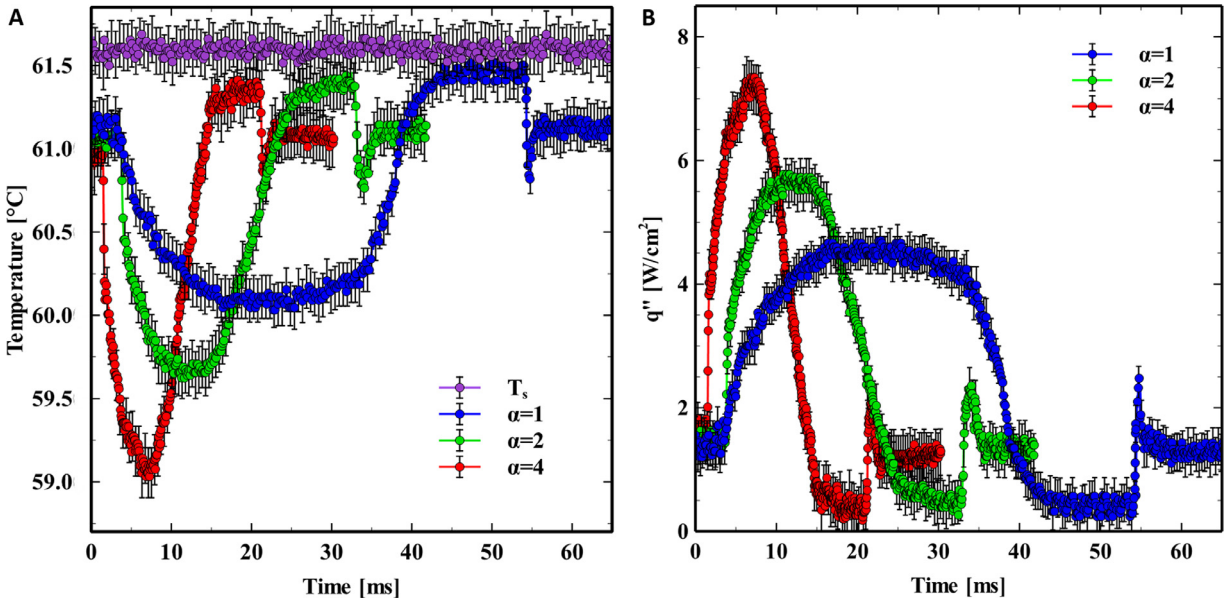

Fig. 7. (A) Temperature and (B) heat flux distributions versus time for three different microchannels with aspect ratios α=1, 2, 4.

since the surface did not experience dryout, i.e. its temperature did not increase, hence a quenching effect and consequently the transient conduction heat transfer mechanism did not occur. For a medium size bubble, the liquid slug moves over sensor S23 after most of the liquid film has evaporated but a complete dryout has not occurred and the drop in the surface temperature (i.e., a rise in surface heat flux) is caused by the bulk liquid arriving on the sensor. Similar to the case of a short bubble, because the surface has not dried out, its temperature has not risen to cause the transient conduction heat transfer mechanism. In the case of a long bubble, the liquid film fully evaporates and surface experiences complete dryout, followed by the transient conduction heat transfer mechanism caused by the quenching effect of the cooler bulk liquid.

3.4. Effect of aspect ratio on thin film evaporation mechanism

Fig. 7 presents temperature and heat flux results as a long bubble passes over a crosswise sensor for channels with cross-sectional dimensions 300 × 75 μm^2, 300 × 150 μm^2, and 300 × 300 μm^2, corresponding to α = 4, 2 and 1, respectively. The tests are conducted such that the Si-SU8 interface temperature for the three channels are identical (T_S =61.6 °C), to allow for an accurate assessment of the effect of channel cross-section geometry on the surface thermal field. The results clearly show a sharper decline in the surface temperature, commensurate with a rise in the surface heat flux, as α is increased, suggesting that the heat transfer coefficient has increased due to the thinning of the liquid film. Reducing the α, results in thickening of the liquid film and a longer evaporation time. For example, it took about 35 ms for the liquid film to evaporate in an α = 1 channel (i.e. the square cross-section channel) whereas 11 ms for that of the α = 4 channel.

3.5. Initial liquid film thickness

After the liquid film is formed, its temperature rapidly changes reaching a quasi-steady state. The initial temperature of the film

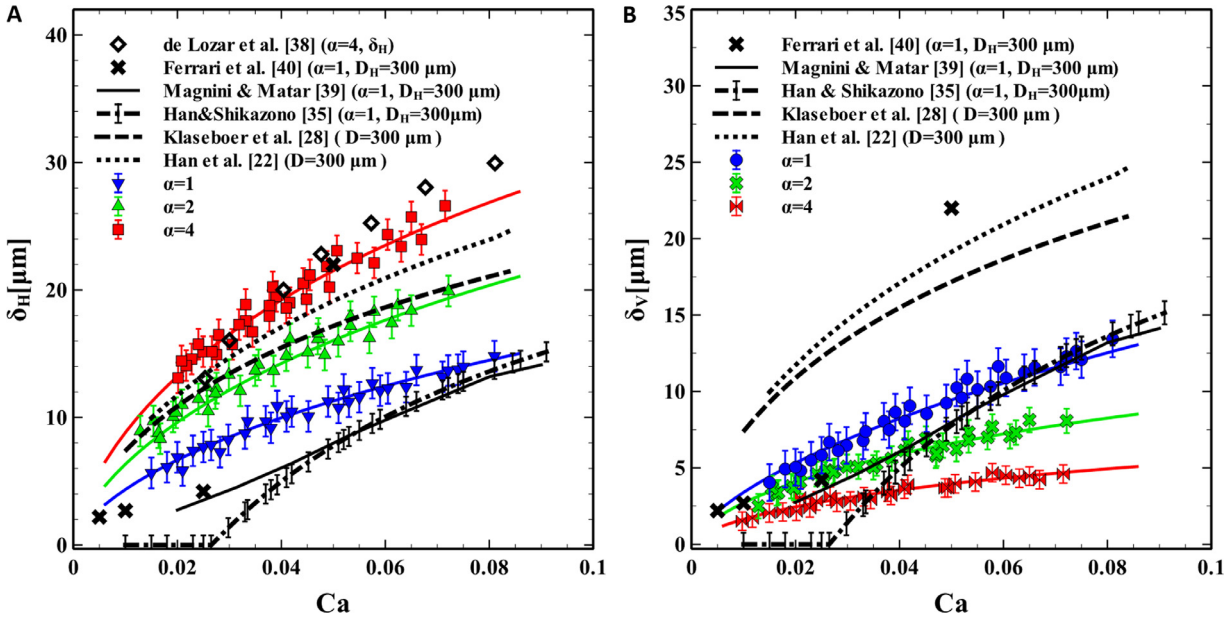

Fig. 8. Variations of the liquid film thickness on (A) the side wall (δ_H) and (B) the bottom wall (δ_V) of the microchannel as a function of *Ca* number and α.

is that of the liquid present on the wall before the film formation, and is assumed to be linear $T(y) = T_s - q''\delta(y)/k$, as validated by Habibi Matin et al. [37]. The initial thickness of the liquid film on the bottom wall can be determined using the surface temperature and heat flux data; $\delta_V = k_{FC-72}(T_{s\_QS} - T_{sat})/q''_{QS} + \int_0^{\Delta t_{init}} (q''(t)/\rho h_{fg})dt$, where q''_{TD} and T_{s-QS} represent the local heat flux and quasi-steady surface temperature, respectively, and Δt_{init} is the time associated with the initial film reaching a quasi-steady temperature (details are discussed in Habibi Matin et al. [37]). In essence, the first term in the expression for δ_V corresponds to the thickness of the liquid film after reaching a quasi-steady temperature, while the second term accounts for the portion of the liquid film evaporated before reaching a quasi-steady temperature.

The liquid thickness on the side walls of the channel (δ_H) is optically measured using the high-resolution images from the microchannel top view. The thickness of both films is a function of *Ca* number and α, as can be seen in Fig. 8. Evidently, thicknesses of both films grow with *Ca* for the three α. However, there is a substantial difference between the thickness of the films and their growth rate with *Ca*, clearly illustrating the fundamental difference between the film thickness in rectangular and circular cross-section channels. The experimental results for δ_H are in a good agreement with the experimetnal results of de Lozar et al. [38] performed for air bubbles fingering into silicone oil and a channel with $\alpha = 4$. The numerical results of Magnini and Matar [39] for the minimum film thickness in square cross-section microchannels can predict the present experimental results for δ_V at $Ca > 0.045$ with less than 15% error; however, at lower *Ca*, their results underestimates the film thickness. Also, optical measurements of the liquid film thickness on the middle of a square channel wall by Han and Shikazono [35] shows a good agreement with the present experiments at Ca > 0.045 but there is a great diagreement at Ca < 0.025 where the film becomes as thin as 5 μm. Further comparisons suggest that neither the modified Bretherton model [28] nor experimental thicknesses obtained for circular cross-section microtubes [22] are able to predict the film thickness in square cross-section microchannels ($\alpha = 1$). The numerical results of Ferrari et al. [40] for the film thickness at 10 × W distance from the bubble's tip are in a reasonable agreement with the present experimental results at Ca ≤ 0.025 while they overestimate the film thickness at higher *Ca*.

Increasing α from 1 to 4, results in an increase in δ_H and a reduction in δ_V. This is due to the fact that bubble confinement in a rectangular microchannel squeezes the bubble into a non-axisymmetric cross-section shape while surface tension acts to restore the vapor–liquid interface to an axisymmetric shape. When α approaches 1, δ_V approaches δ_H.

3.6. Heat transfer coefficient

The heat transfer coefficient associated with the thin film evaporation process can be calculated based on the surface temperature and heat flux data using equation $h(x,t) = q''/(T_s - T_{sat})$. The three-zone heat transfer model of Magnini and Thome [20] uses equation $h(t) = k/\delta(t) = k/(\delta_0 - q''t/\rho h_{fg})$ for estimating the heat transfer coefficient. We used our experimental $Ca = 0.026$, and hydraulic diameters of 120, 200, and 300 μm for channels with α = 4, 2 and 1, respectively, to calculate the initial film thickness (δ_0) using Han et al.'s correlation [22], utilized by Magnini and Thome [20]. Fig. 9 compares the measured heat transfer coefficient on sensor S26 with the three-zone model's predictions. We used average heat fluxes of 3.9, 4.4 and 5.2 W/cm^2 for channels with α =1, 2 and 4, respectively (determined based on the overall heat transfer at the sensor divided by their corresponding evaporation times), in Magnini and Thome's model [20] to calculate *h*. Evidently, the value of *h* approaches infinity as the liquid film thickness (i.e. $\delta_0 - q''t/\rho h_{fg}$) approaches zero. To deal with this singularity, Magnini and Thome [20] assumed that a minimum liquid layer remains on the heater surface (i.e. does not evaporate) – with an amount equal to the surface roughness. The roughness of our surface is on the order of nanometers leading to extremely high *h*. Hence, for the sake of this comparison, we limited the minimum liquid thickness to 5% of its initial value.

As it can be seen, the three-zone model fails to predict the heat transfer coefficient both qualitatively and quantitatively and the discrepancy between the experimental results and the model prediction becomes more pronounced as α increases. The underlying assumption of the three-zone model is that the liquid film formed around the bubble has a uniform initial thickness (δ_0), and its continuous evaporation results in its thinning and consequently

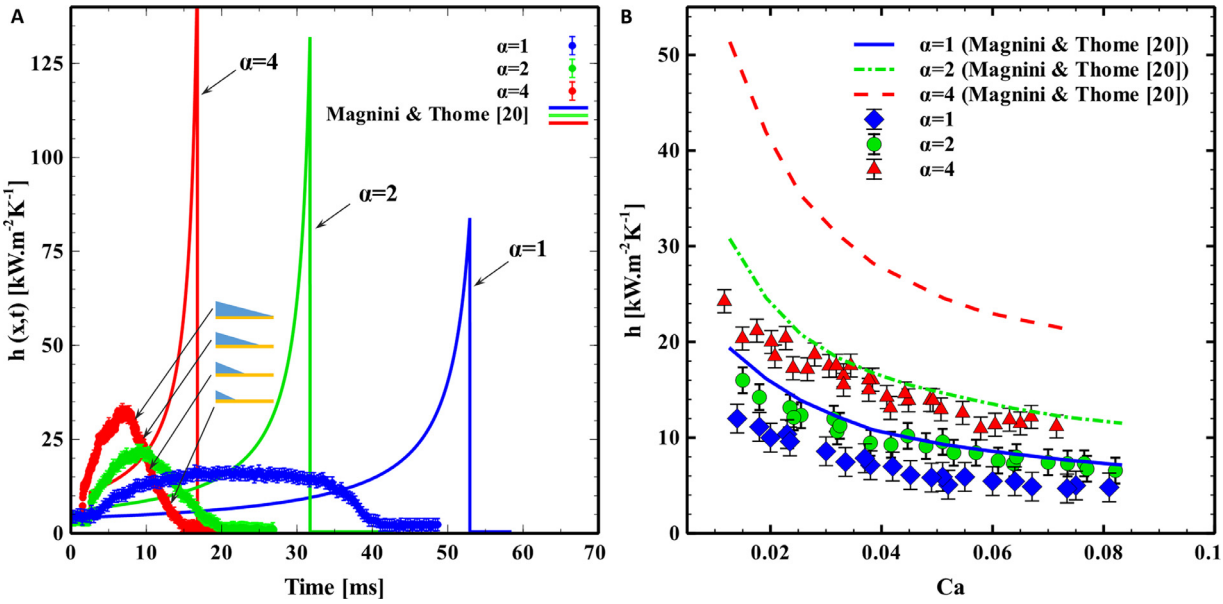

Fig. 9. Comparison between experimental data of sensor S26 and results obtained from the three-zone model [20]: (A) Heat transfer coefficient versus time and (B) Average heat transfer coefficient versus Ca number.

a rapid rise in h. However, a non-uniform liquid film thickness in our rectangular cross-section microchannel has a fundamentally different dryout process, as illustrated in Fig. 9A insets – showing a set of wedge shape thin liquid films depicting the likely dry-out progression process. We believe that h peaks when the liquid film is the thinnest while covering the entire surface area of S26. Thereafter, partial dryout results in continuous decline in h until it diminishes. The average heat transfer coefficients predicted by the model is also compared with the experimental data (Fig. 9B). The film thicknesses implemented in the model are those proposed by Han et al. [22] for circular cross-section microchannels (using the hydraulic diameter). The model's prediction overestimates the experimental data by 50-120% margin depending on the aspect ratio.

4. Conclusion

The heat transfer mechanism associated with the thin film evaporation process in microchannel flow boiling of FC-72 was studied. The local temperature and heat flux variations across the channel width were resolved with unprecedented spatial and temporal resolutions. Since the film thickness around the bubble is not uniform in the rectangular cross-section microchannels, characterization of the thermal field was more complicated than that of the circular cross-section microchannels. Therefore, three microchannels with different α were microfabricated and tested. During the film evaporation process, the non-uniformity of the liquid film led to a gradual dryout starting from the middle of the channel wall, where the liquid film is thinnest. It was shown that the surface heat flux and the initial thickness of the liquid films strongly depend on α. At low α, the liquid film is thicker and it takes longer for it to evaporate. The results also indicate that increasing α, thickens δ_H while δ_V decreases. The results clearly showed that the three-zone model does not apply to all elongated bubbles, and the thin film evaporation process is terminated early in the case of shorter bubbles, as the trailing edge of the bubble advances over the liquid film. Comparison of the present experimental results with the existing model developed by Magnini and Thome [20] suggests that the model fails to predict the heat transfer coefficient for the rectangular cross-section microchannels, both qualitatively and quantitatively. This model assumes that the liquid film formed around the bubble has a uniform initial thickness that evaporates until the entire surface abruptly dries out. Therefore, the model considers dry-out process a sudden event while in the actual experiments it happens gradually. The results of this study paves the way for development of a more accurate mechanistic model for the thin film evaporation heat transfer mechanism in the microchannel flow boiling process.

Declaration of Competing Interest

None.

Acknowledgments

Fabrication of the devices was conducted in the Nanoscale Research Facility (NRF) at the University of Florida. This study was supported by the Office of Naval Research (ONR) under contract N000141912007 with Dr. Mark Spector as the program manager. The authors also acknowledge Morteza Alipanah's assistance in microfabrication of the test device.

References

[1] A.M. Jacobi, J.R. Thome, Heat transfer model for evaporation of elongated bubble flows in microchannels, J. Heat Transf. 124 (2002) 1131, doi:10.1115/1.1517274.
[2] W. Qu, I. Mudawar, Flow boiling heat transfer in two-phase micro-channel heat sinks-I. Experimental investigation and assessment of correlation methods, Int. J. Heat Mass Transf. 46 (2003) 2755–2771, doi:10.1016/S0017-9310(03)00041-3.
[3] M.E. Steinke, S.G. Kandlikar, An experimental investigation of flow boiling characteristics of water in parallel microchannels, J. Heat Transf. 126 (2004) 518, doi:10.1115/1.1778187.
[4] I. Mudawar, Two-phase microchannel heat sinks: theory, applications, and limitations, J. Electron. Packag. 133 (2011) 41002–41031, doi:10.1115/1.4005300.
[5] S.G. Kandlikar, advances History, and challenges in liquid flow and flow boiling heat transfer in microchannels : a critical review, J. Heat Transf. 134 (2012) 034001, doi:10.1115/1.4005126.
[6] S.-M. Kim, I. Mudawar, Theoretical model for local heat transfer coefficient for annular flow boiling in circular mini/micro-channels, Int. J. Heat Mass Transf. 73 (2014) 731–742, doi:10.1016/j.ijheatmasstransfer.2014.02.055.
[7] J.R. Thome, J. Kim, Encyclopedia of two-phase heat transfer and flow II: special topics and applications (A 4-Volume Set), World Scientific, 2015.
[8] C. Li, H.-J. Guo, W.-B. Ye, Y. Hong, S.-M. Huang, Thermohydraulic characteristics of microchannel heat sinks combined with ribs and cavities: effects of geometric parameters and heat flux, Heat Transf. Res. 50 (2019) 89–105, doi:10.1615/HeatTransRes.2018026458.

[9] W.T. Yan, W. Ye, C. Li, Effect of aspect ratio on saturated boiling flow in microchannels with nonuniform heat flux, Heat Transf. - Asian Res. (2019) 3312–3327, doi:10.1002/htj.21543.
[10] W.-T. Yan, C. Li, W.-B. Ye, Y. Hong, S.-M. Huang, The effect of aspect ratio on hydraulic and heat transfer characteristics in a fractal microchannel, Int. J. Fluid Mech. Res. 47 (2020) 71–84, doi:10.1615/InterJFluidMechRes.2019028306.
[11] S.G. Kandlikar, P. Balasubramanian, An extension of the flow boiling correlation to transition, laminar, and deep laminar flows in minichannels and microchannels, Heat Transf. Eng. 25 (2004) 86–93, doi:10.1080/01457630490280425.
[12] S.S. Bertsch, E.A. Groll, S.V. Garimella, A composite heat transfer correlation for saturated flow boiling in small channels, Int. J. Heat Mass Transf. 52 (2009) 2110–2118, doi:10.1016/j.ijheatmasstransfer.2008.10.022.
[13] T. Harirchian, S.V Garimella, Flow regime-based modeling of heat transfer and pressure drop in microchannel flow boiling, Int. J. Heat Mass Transf. 55 (2012) 1246–1260, doi:10.1016/j.ijheatmasstransfer.2011.09.024.
[14] W. Qu, I. Mudawar, Flow boiling heat transfer in two-phase micro-channel heat sinks—II. Annular two-phase flow model, Int. J. Heat Mass Transf. 46 (2003) 2773–2784, doi:10.1016/S0017-9310(03)00042-5.
[15] J.R. Thome, V. Dupont, A.M. Jacobi, Heat transfer model for evaporation in microchannels. Part I: presentation of the model, Int. J. Heat Mass Transf. 47 (2004) 3375–3385, doi:10.1016/j.ijheatmasstransfer.2004.01.006.
[16] S. Bigham, S. Moghaddam, Microscale study of mechanisms of heat transfer during flow boiling in a microchannel, Int. J. Heat Mass Transf. 88 (2015) 111–121, doi:10.1016/j.ijheatmasstransfer.2015.04.034.
[17] S. Bigham, S. Moghaddam, Role of bubble growth dynamics on microscale heat transfer events in microchannel flow boiling process, Appl. Phys. Lett. (2015) 107, doi:10.1063/1.4937568.
[18] M.H. Matin, S. Moghaddam, Prediction of regime transition in two phase flow microchannels based on ultrathin liquid film interfacial instability, in: Proceedings of the 18th IEEE Intersoc. Conf. Therm. Thermomechanical Phenom. Electron. Syst., 2019, pp. 1190–1196, doi:10.1109/ITHERM.2019.8757264.
[19] A. Inoue, K. Moriyama, Thickness of the liquid film formed by a growing bubble in a narrow gap between two horizontal plates, J. Heat Transfer 118 (1996) 132–139, doi:10.1115/1.2824026.
[20] M. Magnini, J.R. Thome, An updated three-zone heat transfer model for slug flow boiling in microchannels, Int. J. Multiph. Flow. 91 (2017) 296–314, doi:10.1016/j.ijmultiphaseflow.2017.01.015.
[21] Y. Han, N. Shikazono, Measurement of the liquid film thickness in micro tube slug flow, Int. J. Heat Fluid Flow. 30 (2009) 842–853, doi:10.1016/j.ijheatfluidflow.2009.02.019.
[22] Y. Han, N. Shikazono, N. Kasagi, The effect of liquid film evaporation on flow boiling heat transfer in a micro tube, Int. J. Heat Mass Transf. 55 (2012) 547–555, doi:10.1016/j.ijheatmasstransfer.2011.11.005.
[23] F.P. Bretherton, The motion of long bubbles in tubes, J. Fluid Mech 10 (1961) 166–188, doi:10.1017/S0022112061000160.
[24] J. Ratulowski, H.C. Chang, Marangoni effects of trace impurities on the motion of long gas-bubbles in capillaries, J. Fluid Mech 210 (1990) 303–328, doi:10.1017/S0022112090001306.
[25] H. Wong, C.J. Radke, S. Morris, Motion of long bubbles in polygonal capillaries. Part 1. Thin films, J. Fluid Mech. 292 (1995) 71–94, doi:10.1017/S0022112095001443.
[26] A. Oron, S.H. Davis, S.G. Bankoff, Long-scale evolution of thin liquid films, Rev. Mod. Phys. 69 (1997) 931–980, doi:10.1103/RevModPhys.69.931.
[27] P. Aussillous, D. Quere, Quick deposition of a fluid on the wall of a tube, Phys. Fluids. 12 (2000) 2367–2371, doi:10.1063/1.1289396.
[28] E. Klaseboer, R. Gupta, R. Manica, An extended Bretherton model for long Taylor bubbles at moderate capillary numbers, Phys. Fluids. 26 (2014) 032107, doi:10.1063/1.4868257.
[29] Y. Sun, C. Guo, Y. Jiang, T. Wang, L. Zhang, Transient film thickness and microscale heat transfer during flow boiling in microchannels, Int. J. Heat Mass Transf. 116 (2018) 458–470, doi:10.1016/j.ijheatmasstransfer.2017.09.027.
[30] C. Guo, J. Tao, Y. Jiang, Y. Sun, T. Wang, Measurement and theoretical analysis of transient liquid film during micro-channel flow boiling, Int. J. Multiph. Flow. 130 (2020) 103365, doi:10.1016/j.ijmultiphaseflow.2020.103365.
[31] A.L. Hazel, M. Heil, The steady propagation of a semi-infinite bubble into a tube of elliptical or rectangular cross-section, J. Fluid Mech. 470 (2002) 91–114, doi:10.1017/S0022112002001830.
[32] T. Taha, Z.F. Cui, CFD modelling of slug flow inside square capillaries, Chem. Eng. Sci. 61 (2006) 665–675, doi:10.1016/j.ces.2005.07.023.
[33] T. Abadie, J. Aubin, D. Legendre, C. Xuereb, Hydrodynamics of gas – liquid Taylor flow in rectangular microchannels, Microfluid. Nanofluidics. 12 (2012) 355–369, doi:10.1007/s10404-011-0880-8.
[34] S. Khodaparast, O. Atasi, A. Deblais, B. Scheid, H.A. Stone, Dewetting of thin liquid films surrounding air bubbles in microchannels, Langmuir 34 (2018) 1363–1370, doi:10.1021/acs.langmuir.7b03839.
[35] Y. Han, N. Shikazono, Measurement of liquid film thickness in micro square channel, Int. J. Multiph. Flow. 35 (2009) 896–903, doi:10.1016/j.ijmultiphaseflow.2009.06.006.
[36] A. De Lózar, A. Juel, A.L. Hazel, The steady propagation of an air finger into a rectangular tube, J. Fluid Mech. 614 (2008) 173–195, doi:10.1017/S0022112008003455.
[37] M. Habibi Matin, A. Fazeli, S. Moghaddam, Thermographic characterization of thin liquid film formation and evaporation in microchannels, Lab Chip 19 (2019) 2610–2618, doi:10.1039/c9lc00301k.
[38] A. De Lózar, A.L. Hazel, A. Juel, Scaling properties of coating flows in rectangular channels, Phys. Rev. Lett. 99 (2007) 234501, doi:10.1103/PhysRevLett.99.234501.
[39] M. Magnini, O.K. Matar, Morphology of long gas bubbles propagating in square capillaries, Int. J. Multiph. Flow. 129 (2020) 103353, doi:10.1016/j.ijmultiphaseflow.2020.103353.
[40] A. Ferrari, M. Magnini, J.R. Thome, Numerical analysis of slug flow boiling in square microchannels, Int. J. Heat Mass Transf. 123 (2018) 928–944, doi:10.1016/j.ijheatmasstransfer.2018.03.012.